Nanostructure Dependence of T-Nb$_2$O$_5$ Intercalation Pseudocapacitance Probed using Tunable Isomorphic Architectures

Wessel van den Bergh, Hasala Lokupitiya, Natalie Alicia Vest, Barry Reid, Stefan Guldin, Morgan Stefik*

Wessel van den Bergh, Dr. Hasala Lokupitiya, Natalie Alicia Vest, Dr. Prof. Morgan Stefik
Department of Chemistry and Biochemistry, University of South Carolina, Columbia, South Carolina 29208, United States.
E-mail: morgan@stefikgroup.com

Dr. Hasala Lokupitiya
Present Address: Department of Chemistry and Biochemistry, College of Charleston, 66 George Street, Charleston, SC 29424, USA

Barry Reid, Dr. Prof. Stefan Guldin
Department of Chemical Engineering, University College London, Torrington Place, London, WC1E 7JE, United Kingdom.

Intercalation pseudocapacitance has emerged as a promising energy storage mechanism that combines the energy density of intercalation materials with the power density of capacitors. Niobium pentoxide was the first material described as exhibiting intercalation pseudocapacitance. The electrochemical kinetics for charging/discharging this material are surface-limited for a wide-range of conditions despite intercalation via diffusion. Investigations of niobium pentoxide nanostructures are diverse and numerous; however, none have yet compared performance while adjusting a single architectural parameter at a time. Such a comparative approach reduces the reliance upon models and the associated assumptions when seeking nanostructure-property relationships. Here we examine a tailored isomorphic series of niobium pentoxide nanostructures with constant pore size and precision

tailored wall thickness. The sweep rate at which niobium pentoxide transitions from being surface-limited to being diffusion-limited is shown to depend sensitively upon the nanoscale dimensions of the niobium pentoxide architecture. Subsequent experiments probing the independent effects of electrolyte concentration and film thickness unambiguously identify solid state lithium diffusion as the dominant diffusion constraint even in samples with just 48.5-67.0 nm thick walls. The resulting architectural dependencies from this type of investigation are critical to enable energy-dense nanostructures that are tailored to deliver a specific power density.

1. Introduction

Electrical energy storage materials with high power density and high energy density are in demand for applications spanning from fast-charging mobile electronics and electric vehicles, to fast-discharge emergency actuators. Each of these examples benefits from high power density. Electric double layer capacitors (EDLCs) and lithium ion batteries (LIBs) do not yet meet the demand for simultaneous energy and power densities. EDLCs' operate based upon surface electrostatic absorption, a rapid short-range mechanism that provides high power density (5-10 kW kg^{-1}) and durability (10^4-10^6 cycles), albeit with relatively low energy density.[1,2] In contrast, batteries are based upon faradaic reactions via intercalation or conversion reactions, providing high energy densities (160 mAh g^{-1} for Li(Ni$_{1/3}$Co$_{1/3}$Mn$_{1/3}$)O$_2$).[3] For such batteries, the power density is generally limited by sluggish solid state diffusion, resulting in low power densities.

Pseudocapacitance, in contrast, combines a faradaic charge storage mechanism with rapid surface-limited kinetics, enabling high energy density and high power density simultaneously. Early pseudocapacitors, such as RuO$_2$[4], relied on reversible surface redox reactions that were highly dependent upon the surface architecture. Recently, a new behavior termed intercalation pseudocapacitance was reported where these surface-limited faradaic

2

reactions extend through the volume of material.[5] $T-Nb_2O_5$ was the first material identified as exhibiting intercalation pseudocapacitance, which was attributed to the lack of a crystallographic phase change combined with its relatively fast solid state diffusion of lithium. In this example, $T-Nb_2O_5$ combined a capacity 130 mAh g^{-1} with a high power rate of 10C, corresponding to a 6-minute charge/discharge time. There remains a need to achieve such high rates within device architectures that have a significant weight and volume fraction of active material,[6–12] a task that requires knowledge of nanostructure-performance relationships to carefully balance multiple transport processes.

All electrochemical reactions, including intercalation pseudocapacitance, rely upon the concomitant transport of electrons, the transport of ions, and the interconversion between reduced and oxidized states. With lithiation of $T-Nb_2O_5$ the steps include a surface step where the lithium traverses between electrolyte and $T-Nb_2O_5$ and also include three diffusion steps: ion transport through the electrolyte, electron transport through the electrode, and lithium intercalation through $T-Nb_2O_5$ (Scheme 1). It follows that the electrochemical response will depend upon the relative rates of each of these steps, all of which are influenced by the way the material is organized in space, *i.e.* the nanoscale architecture.[13–19] A wide range of $T-Nb_2O_5$ nanoscale architectures[20,21] have been investigated to date with most demonstrations including remarkable charge/discharge rates. Materials architectures investigated to-date include nanoparticles,[8,22–25] nanotubes,[12,26,27]nanofibers,[28] nanorods,[29,30] nanowires,[6,31] nanosheets,[9,10,32–37] nanocomposites,[38–44] and related nanostructures.[7,37,45–54] Only few of the above works attempted a rational performance comparison of different nanostructures.[23,52–54] These studies relied on either the simultaneous variation of multiple spatial parameters or were based on single parameter architectures, thus obfuscating the study of nanostructure-property relationships. Prior works on $T-Nb_2O_5$ have also included theoretical studies,[55] comparisons of different crystallographic phases,[36,53,56] and correlated

3

the high diffusion coefficient of Li in T-Nb_2O_5 with its crystallographic features.[8,57,58] In contrast to recent reports of rapid lithium intercalation into nanostructured T-Nb_2O_5, the first investigation of this system by Bard *et al* in 1981 without deliberate nanoscale porosity resulted in a sluggish electrochemical response, requiring 24 hrs for lithium intercalation to complete.[59] This body of works demonstrates that one should reasonably expect the electrochemical kinetics of T-Nb_2O_5 to depend upon the dimensions of the architectural features albeit without yet clear correlations to specific architectural features.

A novel nanomaterial synthesis approach termed persistent micelle templates (PMT) was recently developed to produce materials with tailored series of isomorphic architectures with nanoscale pores.[60–64] Here, block polymers form micelles that serve as templates for material precursors. Subsequent thermal processing converts the precursors to crystalline materials while the removal of the polymer produces a well-defined porosity. Conventional approaches involving micelle templates typically exhibit a dependence of the micelle size on the amount of material precursor, convolving alterations to both the pore size and wall thickness simultaneously. In contrast, PMT relies upon kinetic-control of the template size where variation of the amount of material precursors results in monotonic variation of the wall thickness alone. Thus, PMT enables the synthesis of sample series with constant pore size and tailored wall thickness. Furthermore, since the spherical micelles are kinetically trapped, the resulting series is isomorphic owing to simple sphere packing. The use of an isomorphic series, with constant morphology eliminates tortuosity changes[15,65–71] that come with transitions to cylindrical, lamellar, and other bulk block polymer morphologies.[72] In this work we investigate the electrochemical kinetics within a tailored and systematic series of niobium pentoxide nanostructures. We show that the transition of niobium pentoxide from surface limited kinetics towards diffusion limited kinetics is controlled by the underlying

nanoscale architecture. The methodology described herein relaxes the dependence upon models and enables the evaluation of the rate-sensitivity of each diffusion process.

2. Results and Discussion

The effect of specific feature dimensions on the capability of material to exhibit rapid intercalation pseudocapacitance remains challenging to identify. Understanding these nanostructure dependencies would enable designer nanomaterials where each architectural feature is deliberately tailored to meet the specific power and energy requirements. A general challenge when probing devices with electrochemical analytical methods is ambiguity in identifying the specific diffusion process that corresponds to a rate-dependent response, particularly when multiple diffusive processes have similar rates as is typical for the sake of high energy density. This challenge will now be elaborated in the contexts of four popular analytical approaches. For cyclic voltammetry (CV), the current response, I, varies with a power-dependence of voltage sweep rate, v, where devices are either surface-limited ($I \propto v$), semi-infinite diffusion-limited ($I \propto v^{0.5}$), or a convolution thereof.[73] Although this approach can identify transitions between these regimes, it cannot alone determine the underlying diffusive process. Likewise, impedance spectroscopy data are often interpreted using equivalent circuits where a set of resistors, capacitors, diffusion elements, and other circuit elements represent the electrochemical system. Though quantitative and informative, a significant drawback is that the resulting Nyquist plots are often equally well fitted by multiple equivalent circuits. Even after selecting a circuit model, Nyquist interpretation is often ambiguous as to which of the fitted values correspond to each underlying process.[74–84] Furthermore, equivalent circuits neglect non-uniform ion/electron concentrations throughout the electrode and electrolyte.[80–84] An alternative approach using physicochemical models can numerically address non-uniform concentration gradients, enabling unequivocal interpretations of EDLC[84,85] and pseudocapacitive materials[83,86] from cyclic voltammetry

and impedance spectroscopy, albeit one needs to already have a large number of known parameters. Physicochemical models are also challenging to apply to realistic architectures since even simple 3D geometries required a computational cluster for the calculations.[85] Another analysis method based on 3D Bode plots was recently applied to T-Nb_2O_5 to identify rate constants and diffusion limitations.[87] This study noted that there was either a semi-infinite diffusion limitation of lithium intercalating into the Nb_2O_5 lattice or a diffusion limitation of electrolyte ions reaching the electrode-electrolyte interface. However, the applied analytical technique was unable to distinguish between these two possibilities. The above studies highlight the general deconvolution challenge for all of the above electrochemical analyses. Here we describe the use of a simple approach that resolves this ambiguity by using a series of nanoscale architectures where a single spatial variable is altered at a time to clearly isolate cause and effect.

Persistent micelle templates were used to prepare a tailored set of porous T-Nb_2O_5 samples. The use of custom block polymers and carefully controlled solution conditions enables the self-assembly of micelle templates under kinetic-control where chain exchange between micelles is suppressed and the resulting materials thus have a constant pore size distribution.[62] Electron micrographs of representative samples are shown in **Figure 1** as a function of the ratio of final material mass relative to the micelle template (M:T ratio). Visible in these images is the relatively constant pore size of 109 nm and increasing wall thickness from 48.5 to 67.0 nm corresponding to the increasing M:T ratio. These statistically significant SEM metrics from **Figure 2** are summarized in **Table 1**. The SEM images also reveal the dominant short-range ordering, consistent with randomly packed spheres. The electron micrographs (**Figure S1**) also clearly revealed that the porosity had an open and interconnected network with at least 4 layers of pores apparent from the top view. Such solution processed films typically exhibit compression in the out-of-plane direction since the

6

heat treatments induce contraction.[62,88,89] Thus these films are expected to exhibit ~5 pores across the film thickness based upon cross-sectional SEM of similar samples.[62] Small-angle X-ray scattering (SAXS) of these samples generally had a primary observed peak with a secondary shoulder having an approximate q-ratio of 1:2, also consistent with randomly packed spheres.[90] The main SAXS peak shifts to lower q-spacing as the M:T ratio increases (**Figure 3**), consistent with the expected lattice expansion predicted by the previously established paracrystalline micelle core template (MCT) model (**Equations S1-S3, Table S2**).[61,63] The corresponding shifting d-spacings are shown in Table 1. The resulting best-fit also closely matched the SEM values for wall thickness with a goodness of fit R^2=0.95 (Figure 2a). The GIWAXS measurements confirmed all the Nb_2O_5 samples to be crystalline and consistent with the orthorhombic crystal structure (PDF No. 01-071-0336) of T-Nb_2O_5 (**Figure 4**). Scherrer analysis of these diffractograms indicated all samples had a nominal crystallite size of ~12 nm (see Table 1). Thus a tailored series of isomorphic T-Nb_2O_5 architectures were prepared for electrochemical investigation.

The electrochemical behavior of each sample was investigated using CV over a range of voltage sweep rates. All samples exhibited qualitatively similar CV curves from 2.0 to 1,000 mV s^{-1}. We will first describe the CV characteristics for sample MT1.2 before making comparisons across various sample architectures. The CV curves of MT1.2 (**Figure 5**) exhibit a box-like shape that is characteristic of pseudocapacitance, having broad peaks with narrow separation between the anodic and cathodic peaks. For example, the 2 mV s^{-1} sweep had an anodic peak at 1.826 ± 0.003 V vs Li/Li$^+$ with the corresponding cathodic peak at 1.811 ± 0.001 V vs Li/Li$^+$ in addition to a second broad cathodic peak at 1.559 ± 0.004 V vs Li/Li$^+$ as expected for nanoscale T-Nb_2O_5.[8,32] Please note that the correspondence of these peaks to specific events remains an open topic of investigation outside the scope of this manuscript.[55–57] Faster sweep rates increased the peak separation gradually from 16.3 ± 4.0 mV at 2 mV s^{-1}

to 627.9 ± 22.0 mV at 200 mV s^{-1}, particularly apparent CVs with normalized current (Figure 5b). Sweep rates exceeding 100 mV s^{-1} exhibited sufficient cathodic shift for the cathodic peak to be non-visible within the voltage window. The trends in anodic peak position are shown for all sweep rates in **Figure S2**. All sample conditions, with wall thickness from 48.5 $\pm$ 1.0 to 67.0 ± 1.1 nm were measured by CV. Selected sweep rates are shown in **Figure 6** comparing the sample conditions with these different wall thicknesses. The CV trends reveal monotonically increasing peak separation with wall thickness (increasing M:T ratio) and is suggestive of an increasing diffusion limitation, *vide infra* (Figure 5b and Figure S2). This isomorphic series also exhibited a corresponding trend where the samples with lowest M:T ratio sustained faster sweep rates before lithiation capacity decreases (**Figure S3**). The nominal capacities averaged 364.8 ± 7.7 C g^{-1} Nb$_2$O$_5$. While all samples exhibited pseudocapacitive behavior, further inquiry was needed to explain the performance differences.

The type of rate governing process was assessed using the rate-dependence of the CV responses. The rate governing step was determined using the previously described power-law relation. Here the rate dependence of the peak current is:

$$I = v^b \tag{1}$$

where I is the current, v is the sweep rate, and b corresponds to a power law relationship.[91] Surface-limited processes such as capacitance exhibit a current that is directly proportional to the sweep rate (b=1). In contrast, diffusion-limited processes (semi-infinite) exhibit a current response that is proportional to the square root of sweep rate (b=0.5). The anodic peak current as a function of sweep rate is shown in **Figure 7a** on a log-log scale where the local slope corresponds to the b-value at each sweep rate. The derivative of this graph is thus the rate-dependent b-value that identifies transitions in the type of rate governing process (**Figure 7b**). For example, sample MT1.2 maintains b>0.9 from 2-100 mV s^{-1}, consistent with a surface-limited process. Further increasing the sweep rate leads to monotonic decline of the b-value,

reaching $b=0.64 \pm 0.004$ at 1,000 mV s^{-1}, consistent with a transition towards a semi-infinite diffusion-limited process. Again, we note that b-values non-proximal to 1.0 or 0.5 are ambiguous to interpret, *i.e.* a convolution of multiple rate-limiting processes, and thus limit the discussion to the transition points of $b=0.9$ and $b=0.6$. These values then indicate the thresholds for the maximum v for a surface-limited response ($b>0.9$) as well as the minimum v for a semi-infinite diffusion-limited response. We term these two conditions as the Surface-Limited Threshold (SLT) and the Diffusion-Limited Threshold (DLT). We note that all samples, when measured at sweep rates maintaining $b>0.9$, exhibited greater than 95% relative lithiation capacity with respect to that measured at the slowest sweep rate of 2 mV s^{-1}. Thus, the SLT for any sample serves as a proxy for the onset of capacity loss, *i.e.* "rate-sensitivity." The trends between samples with different wall thicknesses (Figure 7b) show that conditions with higher M:T ratios are increasingly rate-sensitive (**Table 2**). For example, sample condition MT1.2 had a SLT of $v=114.60 \pm 0.48$ mV s^{-1} whereas MT3.0 had a SLT of $v=37.77 \pm 0.27$ mV s^{-1}; that is a factor of 3 change in SLT despite just an 18.5 nm change in wall thickness. This trend, however, is consistent with two possible interpretations: either 1) the diffusive lithium intercalation is rate-limiting, or 2) the ion transport in the electrolyte is rate-limiting since the pore volume fraction decreases as the M:T ratio increases (**Scheme 1**). With any porous system, two independent degrees of freedom exist: e.g. pore size and wall thickness, where their adjustment results in variation of other dependent descriptors such as the volume fraction of pores and the volume fraction of material. This ambiguity is next addressed with additional single-variable experiments.

As depicted in **Scheme 1**, there are three diffusion-based processes: ion transport by the electrolyte through the pores, electron transport along the walls, and lithium intercalation into the walls. The sensitivity towards the first two processes was probed by altering the electrolyte concentration and film thickness respectively. The next set of experiments repeated

the same rate-dependent CV analysis with a 50% reduced electrolyte concentration of 0.5 M

(**Figure 8**). The rate-dependence of the b-values are nearly identical for 1 M and 0.5 M

measurements for both samples MT1.2 and MT3.0, only having minor variations within the

error of the calculations. Thus, it can be concluded that the diffusion-limited process observed

above is not associated with the electrolyte. Please note that all sample comparisons made

above used porous T-Nb_2O_5 films with comparable thickness (Table 2). Next the performance

dependence upon film thickness was examined. Here, increasing the film thickness will

increase both the average electrolyte path length as well as the average electron path length

(Scheme 1). Having excluded sensitivity of these samples towards electrolyte resistance,

differences found herein can be attributed to electron transport alone. Slower spin coating

speeds were thus used to prepare thicker analogs of the films presented above (Table 2). For

condition MT1.2, increasing the film thickness by 13.2% caused the SLT to decrease by

34.4% to v=75.12 ± 0.22 mV s^{-1} (Table 2 and **Figure 9a**). Similarly, with condition MT3.0,

increasing the film thickness by 150% caused the SLT to decrease by 36.4% (**Figure 9b**).

This moderate effect of film thickness is attributable to the diffusive transport of electrons

through the film. In contrast, the previously described 3x change in SLT with wall thickness

alone was a far more significant effect. In summary, the architectures examined here had the

SLT largely determined by the intercalation length scale, the SLT had a minor dependence

upon the electron transport distance, and the samples were free from electrolyte transport

limitations (no SLT dependence).

The SLT values, as well as the sweep rate at other b-values were compared as a

function of the wall-thickness. Here, it is convenient to divide the voltage window by the

sweep rate to yield the sweep time for a particular b-value. Time dependent diffusion

processes follow Fick's second law where the one-dimensional diffusion length with infinite

source is:

$$x = \sqrt{Dt} \qquad\qquad\qquad (2)$$

where x is the diffusion length (half the concentration of the source), D is the diffusion coefficient, and t is time. Thus, a plot of $t^{0.5}$ versus diffusion length yields a straight line. This relationship is used to approximate the time dependence upon intercalation length scale. When considering half of the wall thickness as the diffusion length, we find remarkably linear trends from b=0.6-0.9, with corresponding R^2 values >0.97 (**Figure 10**). As expected for a diffusion-based process, the length-time relationship for the DLT is well modeled by **Equation 2**. Interestingly, the length-time dependence of the SLT is equally well fitted by Equation 2. These data suggest that the relative value of the SLT reflects a balance of a surface process and a diffusive process. Furthermore, we note that the best-fit lines in Figure 10 enable one to choose the length scale needed for a particular time-dependent behavior, assuming there are no other kinetic constraints. This length-scale dependent correlation thus enables one to "nano-optimize" a device for a specific performance target. The numerous correlations presented here highlight that T-Nb_2O_5 intercalation pseudocapacitance is an extrinsic property that depends delicately on the dimensions of the porous architecture.

3. Conclusion

Devices that combine intercalation with pseudocapacitance are attractive for applications needing high energy and power density simultaneously. Orthorhombic niobium pentoxide stands out as the first material termed as exhibiting intercalation pseudocapacitance, yet its performance dependence upon nanoscale feature sizes has remained ambiguous. All intercalation-based charging mechanism involve charges entering a surface and subsequent diffusion into the material. Many electrochemical analytical methods struggle to unambiguously deconvolve these contributions since diffusion-limited steps often exhibit similar time-dependent responses. The studies of T-Nb_2O_5 to date have used either 1) a single

11

nanoscale architecture or 2) a set of nanoscale architectures with multiple spatial variables changing for each sample. Here we demonstrate the use of persistent micelle templates to prepare a series of tunable isomorphic architectures that enable the variation of single spatial variable at a time. This approach reduces the dependence upon models and can establish unambiguous nanostructure-property relationships. Two regime transitions were identified, the maximum sweep rate for surface-limited kinetics (Surface-Limited Threshold) and the minimum sweep rate for diffusion-limited kinetics (Diffusion-Limited Threshold). For the T-Nb_2O_5 architectures investigated here, it was revealed that both the SLT and DLT sensitively depend upon the intercalation length-scale, have a moderate dependence on the electron transport length, and were not affected by electrolyte transport constraints. These types of performance dependencies upon architecture are critical to enable energy-dense nanostructures that are "nano-optimized" to deliver a specific power density.

4. Experimental Section/Methods

Materials. Ethanol (EtOH 200 proof, 100%, Fisher) was dried at room temperature by storage over 30% w/v of molecular sieves (3Å, 8-12 mesh, Acros Organics) for a week.[92] Concentrated hydrochloric acid (HCl, 37% w/w, ACS grade, VWR) and (HCl, 37% w/w, trace metal grade, Fisher Scientific), concentrated hydrofluoric acid (HF, 48% w/w, trace metal grade, Sigma-Aldrich), poly(ethylene glycol)methyl ether (PEO-OH, M_n = 20,000 gmol^{-1}, Aldrich), 2-bromopropionic acid (>99%, Aldrich), and 4-(dimethylamino) pyridine (99%, Aldrich) were used as received. Niobium(V) Ethoxide (NbOEth, 99.9%, Fisher), copper(I) bromide (99.99%, Aldrich), tris-(2-dimethylaminoethyl) amine (97%, Aldrich), anhydrous lithium perchlorate (LiClO$_4$, 99.99%, Aldrich), concentrated nitric acid (HNO$_3$, 70%, Fisher Scientific), and anhydrous propylene carbonate (99.7%, Aldrich) were used as received and stored inside a glove box. Hexyl acrylate (96%, VWR) monomer was passed through a basic

alumina column just prior to use. Chloroform (>99%, Aldrich), hexane (>98.5%, Fisher), tetrahydrofuran (Fisher), and dimethylformamide (97%, Aldrich) were used as received.

Polymer synthesis. Poly(ethylene oxide-*b*-hexyl acrylate), PEO-*b*-PHA, diblock polymer was synthesized by a two-step synthesis. A Steglich esterification of poly(ethylene glycol)methyl ether was used to form a macroinitiator, followed by atom transfer radical polymerization (ATRP) to grow the PHA block. The procedure is described elsewhere in detail.[60] The molar mass of PHA was determined using a Bruker Avance III HD 300 ^{1}H NMR by comparison to the known PEO (M_n = 20.0 kg mol^{-1}) (**Figure S4a** and **Table S1**). The molar mass dispersity was characterized using a Waters gel permeation chromatograph (GPC) equipped with a Waters 1525 binary pump, three styragel columns (HR1, HR3, HR5 in the effective molecular weight range of 0.1-5, 0.5-30, and 2-400 kg mol^{-1}, respectively), and a Waters 2414 refractive index detector. The GPC was calibrated with poly(styrene) standards (1.50, 3.28, 10.00, 17.40, 32.70, 120.00, 214.00, 545.00, 1010.00 kg mol^{-1}) obtained from Polymer Standards Service GmbH. GPC samples were prepared in THF at concentrations of 5 mg mL^{-1}, filtered through a 0.2 μm syringe filter prior to injection (**Figure S4b** and Table S1).[62,93]

Synthesis of Porous Materials with Persistent Micelle Templates. A micelle stock solution was prepared by dispersing PEO-*b*-PHA (25 mg) in EtOH (2.5 mL) at room temperature with gentle agitation. Then to ensure full dissolution, the 20 mL scintillation vial for each solution was placed in an oven at 80 ºC for 30 min and was subsequently cooled to room temperature overnight. Concentrated HCl (~0.060 g) was added slowly to reach 1.8 wt% with respect to the total mixture (PEO-*b*-PHA, EtOH, and HCl). We note that ethanol was recently found to result in minimal microporosity within the final Nb$_2$O$_5$ walls.[61] After acid addition, the solution was placed in a water bath at 35 ºC to maintain dispersion of the polymer micelles. A

prescribed quantity of NbOEth was added to each solution to reach the target Material:Template ratio (M:T).[63] Here the M:T is a mass ratio of the final anticipated Nb_2O_5 mass relative to the mass of block polymer. Each film was spin coated for 30 seconds at 1000, 1500, 2000, and 2150 rpm under 15% relative humidity for each M:T condition of 1.2, 1.8, 2.4, and 3.0 respectively as described in detail elsewhere.[61,63,94] Immediately after the end of spin coating, each sample was removed from the humidity-controlled chamber and placed on a 110 °C hot plate overnight to crosslink the oxide, termed as "aging." The room humidity during aging was not found to have an effect. Aging conditions were optimized to prevent initial dewetting and to assure sufficient oxide connectivity to survive calcination. After each spin coating process, the spin coating chamber (Tupperware) was replaced to avoid effects of residual solvent vapor, as noted previously.[61] Glass, silicon, and FTO substrates were used for SAXS, SEM, and electrochemistry, respectively. After aging, the films were calcined, 5 °C min^{-1} to 200 °C followed by 10 °C min^{-1} to 600 °C with a 1 hr soak.

Electrode Preparation. FTO substrates (TEC-15, Hartford Glass, CT) were rinsed and scrubbed with DI water using Kimwipes until scrubbing produces an audible squeaking noise followed by rinsing and scrubbing with IPA wetted Kimwipes again in the same manner. The substrates were then sonicated in a soapy water bath (2 g/L deconex) for 30 minutes. The water and alcohol scrub and rinse steps were repeated as before. The resulting substrates were stored submerged in IPA until near the time of spin coating. Just prior to coating, the FTO substrates were removed from IPA, blown dry, and then calcined to 450 °C for 3 hr to remove trace organics. After calcination, the FTO substrates were held at 110 °C until the moment they were used for spin coating. An uncoated area for electrical contact was maintained by masking part of the substrate with high temperature Kapton tape (**Figure S5**). After spin coating and aging as described above, the edges of the FTO substrates were cleaved to remove

edge effects[63] where residual template solution can collect at the substrate edges, resulting in a locally varied film thickness. The back of each film was engraved with identifying marks for M:T, recipe number, and film number. The Kapton mask was then removed. The ~1 mm portion of the film proximal to the Kapton mask exhibited an edge effect with local variation of film thickness and was removed by scraping away oxide film with glass prior to calcination (Figure S5). The final active area of each sample was determined by photography over a ruled grid and was analyzed using ImageJ.

X-ray Scattering Experiments. X-ray experiments were conducted using a SAXSLab Ganesha at the South Carolina SAXS collaborative (SCSC). A Xenocs GeniX 3D microfocus source was used with a copper target to produce monochromatic beam with a 0.154 nm wavelength. The instrument was calibrated prior to measurements using National Institute of Standards and Technology (NIST) reference material, 640d silicon powder with peak position at $2\theta =$ 28.44°. A Pilatus 300k detector (Dectris) was used to collect the 2D scattering patterns with nominal pixel dimensions of 172x172 μm. SAXS data were acquired with an X-ray flux of ~1.41 M photon per second upon the sample and a detector-to-sample distance of 1,400 mm. Transmission small-angle X-ray scattering (SAXS) data were measured to observe the purely in-plane morphology. The 2D images were azimuthally integrated to yield the scattering vector and intensity. Peak positions were fitted using custom MATLAB software. Grazing incidence wide-angle X-ray scattering (GIWAXS) measurements were conducted with an incident angle (α_i) of 7° relative to the incident beam. The GIWAXS sample-to-detector distance was 112.1 mm with an X-ray flux of ~39.2 M photon per second upon the sample. The 2D WAXS data were masked to remove diffuse reflectance before integration and analysis of the resulting 1D data. A Gaussian point-spread function was utilized to interpret scattering data as a result of grain-size broadening per the Scherrer formula.[95,96]

Scanning Electron Microscopy (SEM). Top-view images of calcined films were acquired with a Zeiss Ultraplus thermal field emission SEM using an accelerating voltage of 5 keV and an in-lens secondary electron detector. The working distance was maintained at ~3 mm and images were acquired at constant magnification of 300k. At least 100 measurements were made upon each feature (pore and walls) to derive statistical metrics. These measures were conducted in numerous directions on numerous images to yield average values. The wall thickness was measured as the diameter on an inscribed circle between neighboring pores as described elsewhere.[60] Pore size and wall-thickness data are presented as average values with the standard-error-of-the-mean. Cross-sectional SEM was used to determine film thickness.

Inductively Coupled Plasma Mass Spectrometry (ICP-MS). A series of films prepared on FTO substrates were cut to ~1 cm^2 of the Nb_2O_5 coating. A photograph was used to account for the specific substrate area as previously described. These films along with FTO blanks were heated in a Teflon vessel containing 70% HNO_3 (trace metal grade), 37% HCl (trace metal grade), and 48% HF (trace metal grade) (1:3:0.5 mL) respectively at 180 ºC for 12 hours before solutions were diluted with water (18.2 MΩ cm) to 50 mL volume and measured using a Thermo-Finnigan Element XR ICP-MS. The instrument was calibrated using a range of concentrations spanning those of the measured samples in conjunction with FTO blanks. A range of HF contents was screened to assure efficient Nb_2O_5 digestion (**Figure S6**). These data were used to calculate the Nb_2O_5 mass-per-area metric for each sample condition.

Electrochemical Analysis. Electrochemical measurements were conducted using a three-electrode setup with a BioLogic SP-150 potentiostat. All measurements were performed in an argon-filled glovebox (<1 ppm O_2, <1 ppm H_2O). The working electrodes were porous Nb_2O_5

prepared using PMT on FTO substrates as described above. The working electrode was held by a home-built titanium metal clamp to assure ohmic contact to the FTO. All potentials are reported vs a Li/Li$^+$ reference electrode. The counter electrode was also lithium foil approximately 540 mm^2 in surface area. All lithium foils were scraped until shiny just prior to immersion in electrolyte. The electrolyte solution was 1.0 M LiClO$_4$ in propylene carbonate. A series of diagnostic cyclic voltammograms and electric impedance spectroscopy measurements were used to verify ohmic contact. The working electrode was then held at 1.2 V for 20 minutes before cycling from 1.2 V to 3.0 V repeatedly 20 times at 10 mV/s to remove trace contaminants. A series of 28 logarithmically spaced sweeps ranging in rate from 1000 mV s^{-1} to 2 mV s^{-1} were run in sequence starting from 1.2 V vs Li/Li$^+$. There was a 3 min hold period at the end of each sweep to allow the electrode to equilibrate. Mass normalized was based upon the film area and ICP-MS measurements with identical samples.

Supporting Information (For Publication)
Supporting Information is available from the Wiley Online Library or from the author.

Abbreviations

CV, Cyclic Voltammetry; DLT, Diffusion Limited Threshold; EDLCs, Electrical Double-Layer Capacitors; FTO, Fluorine-doped Tin Oxide; GI-WAXS, Grazing Incidence Wide-Angle X-ray Scattering; GPC, Gel Permeation Chromatography; LIBs, Lithium-Ion Batteries; M:T ratio, Material-to-Template Ratio; MCT, Micelle Core Template; PMTs, Persistent Micelle Templates; SEM, Scanning Electron Microscopy; SAXS, Small-Angle X-ray Scattering; SLT, Surface Limited Threshold.

Conflicts of Interest

There are conflicts of interest to declare.

Acknowledgements

References

[1]   A. Borenstein, O. Hanna, R. Attias, S. Luski, T. Brousse, D. Aurbach, *J. Mater. Chem. A* **2017**, *5*, 12653.

[2]   A. G. Pandolfo, A. F. Hollenkamp, *J. Power Sources* **2006**, *157*, 11.

[3]   K. M. Shaju, G. V. Subba Rao, B. V. R. Chowdari, *Electrochim. Acta* **2002**, *48*, 145.

[4]   S. Trasatti, G. Buzzanca, *J. Electroanal. Chem. Interfacial Electrochem.* **1971**, *29*, A1.

[5]   V. Augustyn, J. Come, M. A. Lowe, J. W. Kim, P.-L. Taberna, S. H. Tolbert, H. D. Abruña, P. Simon, B. Dunn, *Nat. Mater* **2013**, *12*, 518.

[6]   H. Yang, H. Xu, L. Wang, L. Zhang, Y. Huang, X. Hu, *Chem. - A Eur. J.* **2017**, *23*, 4203.

[7]   S. Zhang, J. Wu, J. Wang, W. Qiao, D. Long, L. Ling, *J. Power Sources* **2018**, *396*, 88.

[8]   J. W. Kim, V. Augustyn, B. Dunn, *Adv. Energy Mater.* **2012**, *2*, 141.

[9]   S. Lou, X. Cheng, L. Wang, J. Gao, Q. Li, Y. Ma, Y. Gao, P. Zuo, C. Du, G. Yin, *J. Power Sources* **2017**, *361*, 80.

[10] D. Li, J. Shi, H. Liu, C. Liu, G. Dong, H. Zhang, Y. Yang, G. Lu, H. Wang, *Sustain. Energy Fuels* **2019**, *3*, 1055.

[11] J. Lin, Y. Yuan, Q. Su, A. Pan, S. Dinesh, C. Peng, G. Cao, S. Liang, *Electrochim. Acta* **2018**, *292*, 63.

[12] S. Hemmati, G. Li, X. Wang, Y. Ding, Y. Pei, A. Yu, Z. Chen, *Nano Energy* **2019**, *56*, 118.

[13] C. Zhu, R. E. Usiskin, Y. Yu, J. Maier, *Science* **2017**, *358*, eaao2808.

[14] J. W. Long, B. Dunn, D. R. Rolison, H. S. White, *Chem. Rev.* **2004**, *104*, 4463.

[15] A. Vu, Y. Qian, A. Stein, *Adv. Energy Mater.* **2012**, *2*, 1056.

[16] J. Maier, *Faraday Discuss.* **2015**, *176*, 17.

[17] H. Liu, Z. Bi, X.-G. Sun, R. R. Unocic, M. P. Paranthaman, S. Dai, G. M. Brown, *Adv. Mater.* **2011**, *23*, 3450.

[18] J. K. Shon, H. S. Lee, G. O. Park, J. Yoon, E. Park, G. S. Park, S. S. Kong, M. Jin, J. M. Choi, H. Chang, S. Doo, J. M. Kim, W. S. Yoon, C. Pak, H. Kim, G. D. Stucky, *Nat. Commun.* **2016**, *7*, 1.

[19] J. M. Szeifert, J. M. Feckl, D. Fattakhova-Rohlfing, Y. Liu, V. Kalousek, J. Rathousky, T. Bein, *J. Am. Chem. Soc.* **2010**, *132*, 12605.

[20] Q. Deng, Y. Fu, C. Zhu, Y. Yu, *Small* **2019**, *15*, 1804884.

[21] C. Li, Q. Li, Y. V. Kaneti, D. Hou, Y. Yamauchi, Y. Mai, *Chem. Soc. Rev.* **2020**, *49*, 4681.

[22] E. Lim, C. Jo, H. Kim, M.-H. Kim, Y. Mun, J. Chun, Y. Ye, J. Hwang, K.-S. Ha, K. C. Roh, K. Kang, S. Yoon, J. Lee, *ACS Nano* **2015**, *9*, 7497.
[23] X. Ge, C. Gu, Z. Yao, J. Sun, X. Wang, J. Tu, *Chem. Eng. J.* **2018**, *338*, 211.
[24] L. Kong, X. Liu, J. Wei, S. Wang, B. B. Xu, D. Long, F. Chen, *Nanoscale* **2018**, *10*, 14165.
[25] W. Luo, Y. Li, J. Dong, J. Wei, J. Xu, Y. Deng, D. Zhao, *Angew. Chem.* **2013**, *125*, 10699.
[26] Y. Lian, D. Wang, S. Hou, C. Ban, J. Zhao, H. Zhang, *Electrochim. Acta* **2020**, *330*, 135204.
[27] G. Luo, H. Li, D. Zhang, L. Gao, T. Lin, *Electrochim. Acta* **2017**, *235*, 175.
[28] J. Y. Cheong, J.-W. Jung, D.-Y. Youn, C. Kim, S. Yu, S.-H. Cho, K. R. Yoon, I.-D. Kim, *J. Power Sources* **2017**, *360*, 434.
[29] B. Deng, T. Lei, W. Zhu, L. Xiao, J. Liu, *Adv. Funct. Mater.* **2018**, *28*, 1704330.
[30] C. Shi, K. Xiang, Y. Zhu,, X. Chen, W. Zhou, H. Chen, *Ceram. Int.* **2017**, *43*, 12388.
[31] H. Song, J. Fu, K. Ding, C. Huang, K. Wu, X. Zhang, B. Gao, K. Huo, X. Peng, P. K. Chu, *J. Power Sources* **2016**, *328*, 599.
[32] K. Brezesinski, J. Wang, J. Haetge, C. Reitz, S. O. Steinmueller, S. H. Tolbert, B. M. Smarsly, B. Dunn, T. Brezesinski, *J. Am. Chem. Soc.* **2010**, *132*, 6982.
[33] S. Jiang, S. Dong, L. Wu, Z. Chen, L. Shen, X. Zhang, *J. Electroanal. Chem.* **2019**, *842*, 82.
[34] Y. Jiao, H. Zhang, H. Zhang, A. Liu, Y. Liu, S. Zhang, *Nano Res.* **2018**, *11*, 4673.
[35] Y. Li, R. Wang, W. Zheng, Q. Zhao, S. Sun, G. Ji, S. Li, X. Fan, C. Xu, *Mater. Technol.* **2020**, 1.
[36] J. Liao, R. Tan, Z. Kuang, C. Cui, Z. Wei, X. Deng, Z. Yan, Y. Feng, F. Li, C. Wang, J. Ma, *Chinese Chem. Lett.* **2018**, *29*, 1785.
[37] S. Kim, J. Hwang, J. Lee, J. Lee, *Sci. Adv.* **2020**, *6*, eabb3814.
[38] E. Lim, C. Jo, M. S. Kim, M.-H. Kim, J. Chun, H. Kim, J. Park, K. C. Roh, K. Kang, S. Yoon, J. Lee, *Adv. Funct. Mater.* **2016**, *26*, 3711.
[39] P. Nagaraju, R. Vasudevan, A. Alsalme, A. Alghamdi, M. Arivanandhan, R. Jayavel, *Nanomaterials* **2020**, *10*, 160.
[40] M. Y. Song, N. R. Kim, H. J. Yoon, S. Y. Cho, H.-J. Jin, Y. S. Yun, *ACS Appl. Mater. Interfaces* **2017**, *9*, 2267.
[41] L. Kong, C. Zhang, S. Zhang, J. Wang, R. Cai, C. Lv, W. Qiao, L. Ling, D. Long, *J. Mater. Chem. A* **2014**, *2*, 17962.
[42] G. Ma, K. Li, Y. Li, B. Gao, T. Ding, Q. Zhong, J. Su, L. Gong, J. Chen, L. Yuan, B. Hu, J. Zhou, K. Huo, *ChemElectroChem* **2016**, *3*, 1360.
[43] W. Hu, S. Zhang, W. Zhang, M. Wang, F. Feng, *J. Nanoparticle Res.* **2020**, *22*, 57.
[44] H. Sun, L. Mei, J. Liang, Z. Zhao, C. Lee, H. Fei, M. Ding, J. Lau, M. Li, C. Wang, X. Xu, G. Hao, B. Papandrea, I. Shakir, B. Dunn, Y. Huang, X. Duan, *Science* **2017**, 599.
[45] F. Idrees, J. Hou, C. Cao, F. K. Butt, I. Shakir, M. Tahir, F. Idrees, *Electrochim. Acta* **2016**, *216*, 332.
[46] Z. Chen, H. Li, X. Lu, L. Wu, J. Jiang, S. Jiang, J. Wang, H. Dou, X. Zhang, *ChemElectroChem* **2018**, *5*, 1516.
[47] J. Zhai, Y. Wu, X. Zhao, Q. Yang, *J. Alloys Compd.* **2017**, *715*, 275.
[48] J. W. Kim, S. Kim, H. Kim, *Int. J. Energy Res.* **2019**, *43*, 4359.
[49] J. Hu, J. Li, K. Wang, H. Xia, *Electrochim. Acta* **2020**, *331*, 135364.
[50] X. Xu, B. Tian, S. Zhang, J. Kong, D. Zhao, B. Liu, *Anal. Chim. Acta* **2004**, *519*, 31.
[51] E. Lim, H. Kim, C. Jo, J. Chun, K. Ku, S. Kim, H. I. Lee, I.-S. Nam, S. Yoon, K. Kang, J. Lee, *ACS Nano* **2014**, *8*, 8968.
[52] A. L. Viet, M. V. Reddy, R. Jose, B. V. R. Chowdari, S. Ramakrishna, *J. Phys. Chem. C* **2010**, *114*, 664.
[53] S. Li, Q. Xu, E. Uchaker, X. Cao, G. Cao, *CrystEngComm* **2016**, *18*, 2532.
[54] S. Ouendi, C. Arico, F. Blanchard, J.-L. Codron, X. Wallart, P. L. Taberna, P. Roussel, L. Clavier, P. Simon, C. Lethien, *Energy Storage Mater.* **2019**, *16*, 581.

[55] A. A. Lubimtsev, P. R. C. Kent, B. G. Sumpter, P. Ganesh, *J. Mater. Chem. A* **2013**, *1*, 14951.

[56] K. J. Griffith, A. C. Forse, J. M. Griffin, C. P. Grey, *J. Am. Chem. Soc.* **2016**, *138*, 8888.

[57] D. Chen, J.-H. Wang, T.-F. Chou, B. Zhao, M. A. El-Sayed, M. Liu, *J. Am. Chem. Soc.* **2017**, *139*, 7071.

[58] J. Come, V. Augustyn, J. W. Kim, P. Rozier, P.-L. Taberna, P. Gogotsi, J. W. Long, B. Dunn, P. Simon, *J. Electrochem. Soc.* **2014**, *161*, A718.

[59] B. Reichman, A. J. Bard, *J. Electrochem. Soc.* **1981**, *128*, 344.

[60] K. A. Lantz, N. B. Clamp, W. van den Bergh, A. Sarkar, M. Stefik, *Small* **2019**, *15*, 1900393.

[61] A. Sarkar, L. Evans, M. Stefik, *Langmuir* **2018**, *34*, 5738.

[62] H. N. Lokupitiya, A. Jones, B. Reid, S. Guldin, M. Stefik, *Chem. Mater.* **2016**, *28*, 1653.

[63] A. Sarkar, M. Stefik, *J. Mater. Chem. A* **2017**, *5*, 11840.

[64] A. Sarkar, A. Thyagarajan, A. Cole, M. Stefik, *Soft Matter* **2019**, *15*, 5193.

[65] P. Sutton, P. Bennington, S. N. Patel, M. Stefik, U. B. Wiesner, P. F. Nealey, U. Steiner, I. Gunkel, *Adv. Funct. Mater.* **2019**, *29*, 1905977.

[66] R. Dehmel, J. A. Dolan, Y. Gu, U. Wiesner, T. D. Wilkinson, J. J. Baumberg, U. Steiner, B. D. Wilts, I. Gunkel, *Macromolecules* **2017**, *50*, 6255.

[67] O. Kim, S. Y. Kim, J. Lee, M. J. Park, *Chem. Mater.* **2016**, *28*, 318.

[68] P. Docampo, S. Guldin, M. Stefik, P. Tiwana, M. C. Orilall, S. Hüttner, H. Sai, U. Wiesner, U. Steiner, H. J. Snaith, *Adv. Funct. Mater.* **2010**, *20*, 1787.

[69] E. J. W. Crossland, P. Cunha, S. Ludwigs, M. A. Hillmyer, U. Steiner, *ACS Appl. Mater. Interfaces* **2011**, *3*, 1375.

[70] E. J. W. Crossland, M. Nedelcu, C. Ducati, S. Ludwigs, M. A. Hillmyer, U. Steiner, H. J. Snaith, *Nano Lett.* **2009**, *9*, 2813.

[71] M. Nedelcu, J. Lee, E. J. W. Crossland, S. C. Warren, M. C. Orilall, S. Guldin, S. Hüttner, C. Ducati, D. Eder, U. Wiesner, U. Steiner, H. J. Snaith, *Soft Matter* **2009**, *5*, 134.

[72] M. Stefik, J. Song, H. Sai, S. Guldin, P. Boldrighini, M. C. Orilall, U. Steiner, S. M. Gruner, U. Wiesner, *J. Mater. Chem. A* **2015**, *3*, 11478.

[73] H. Lindström, S. Södergren, A. Solbrand, H. Rensmo, J. Hjelm, A. Hagfeldt, S.-E. Lindquist, *J. Phys. Chem. B* **1997**, *101*, 7717.

[74] B. E. Conway, W. G. Pell, *J. Power Sources* **2002**, *105*, 169.

[75] S. Yoon, J. H. Jang, B. H. Ka, S. M. Oh, *Electrochim. Acta* **2005**, *50*, 2255.

[76] O. Bohlen, J. Kowal, D. U. Sauer, *J. Power Sources* **2007**, *172*, 468.

[77] S. Yoon, C. W. Lee, S. M. Oh, *J. Power Sources* **2010**, *195*, 4391.

[78] M. Kaus, J. Kowal, D. U. Sauer, *Electrochim. Acta* **2010**, *55*, 7516.

[79] R. L. Spyker, R. M. Nelms, *IEEE Trans. Aerosp. Electron. Syst* **2000**, *36*, 829.

[80] M. Z. Bazant, K. Thornton, A. Ajdari, *Phys. Rev. E* **2004**, *70*, 021506.

[81] K. T. Chu, M. Z. Bazant, *Phys. Rev. E* **2006**, *74*, 011501.

[82] L. Højgaard Olesen, M. Z. Bazant, H. Bruus, *Phys. Rev. E* **2010**, *82*, 011501.

[83] B.-A. Mei, J. Lau, T. Lin, S. H. Tolbert, B. S. Dunn, L. Pilon, *J. Phys. Chem. C* **2018**, *122*, 24499.

[84] B.-A. Mei, O. Munteshari, J. Lau, B. Dunn, L. Pilon, *J. Phys. Chem. C* **2018**, *122*, 194.

[85] B.-A. Mei, L. Pilon, *Electrochim. Acta* **2017**, *255*, 168.

[86] H.-L. Girard, B. Dunn, L. Pilon, *Electrochim. Acta* **2016**, *211*, 420.

[87] J. S. Ko, C.-H. Lai, J. W. Long, D. R. Rolison, B. Dunn, J. Nelson Weker, *ACS Appl. Mater. Interfaces* **2020**, *12*, 14071.

[88] S. Dutta, K. C.-W. Wu, T. Kimura, *Chem. Mater.* **2015**, *27*, 6918.

[89] S. Guldin, P. Docampo, M. Stefik, G. Kamita, U. Wiesner, H. J. Snaith, U. Steiner, *Small* **2012**, *8*, 432.

[90] C. Robertus, W. H. Philipse, J. G. H. Joosten, Y. K. Levine, *J. Chem. Phys.* **1989**, *90*, 4482.

[91] S. Ardizzone, G. Fregonara, S. Trasatti, *Electrochim. Acta* **1990**, *35*, 263.

[92] D. B. G. Williams, M. Lawton, *J. Org. Chem.* **2010**, *75*, 8351.
[93] L. J. Fetters, D. J. Lohse, D. Richter, T. A. Witten, A. Zirkel, *Macromolecules* **1994**, *27*, 4639.
[94] H. N. Lokupitiya, M. Stefik, *Nanoscale* **2017**, *9*, 1393.
[95] A. L. Patterson, *Phys. Rev.* **1939**, *56*, 978.
[96] P. Scherrer, *Math. Phys.* **1918**, *2*, 98.

Figures
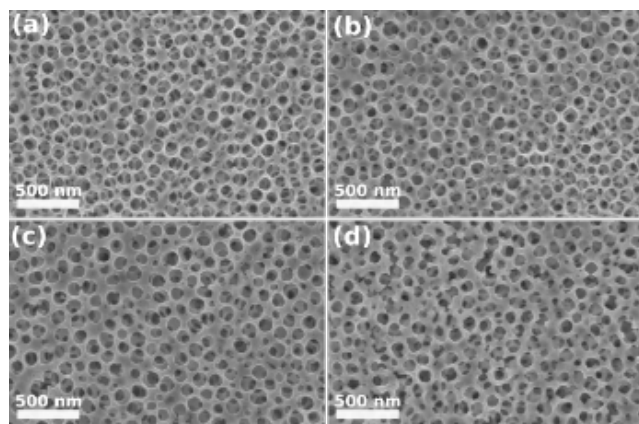
Figure 1. SEM images of isomorphic series of porous samples prepared with persistent micelle templates using different Material:Template ratios: MT1.2 (a), MT1.8 (b), MT2.4 (c), MT3.0 (d).
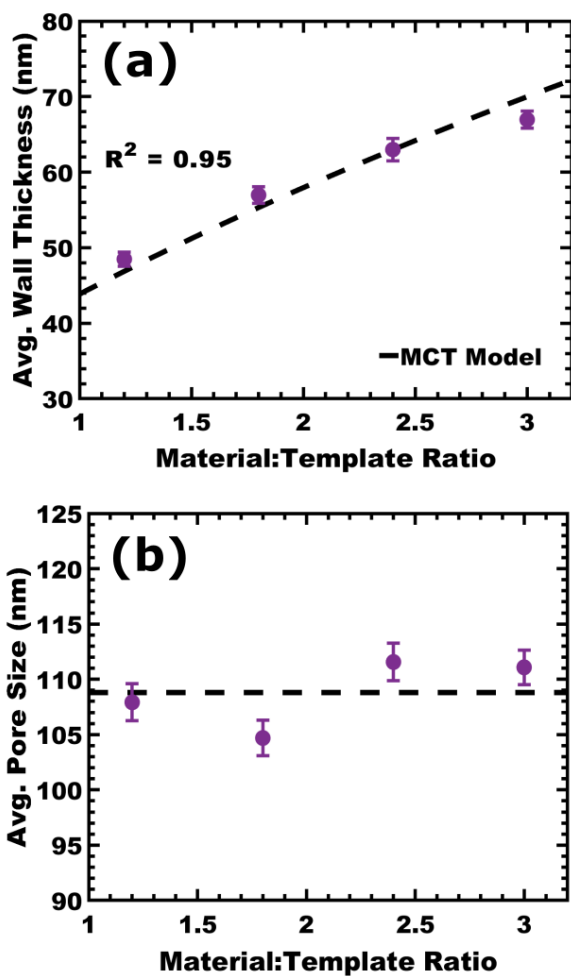
Figure 2. Wall thickness (a) and pore size (b) statistics were measured from SEM images as a function of the Material:Template ratio. The dashed line in (a) corresponds the best fit of the MCT model. The dashed line in (b) is the overall average of the pore diameter. The error bars correspond to the standard-error-of-the-mean.
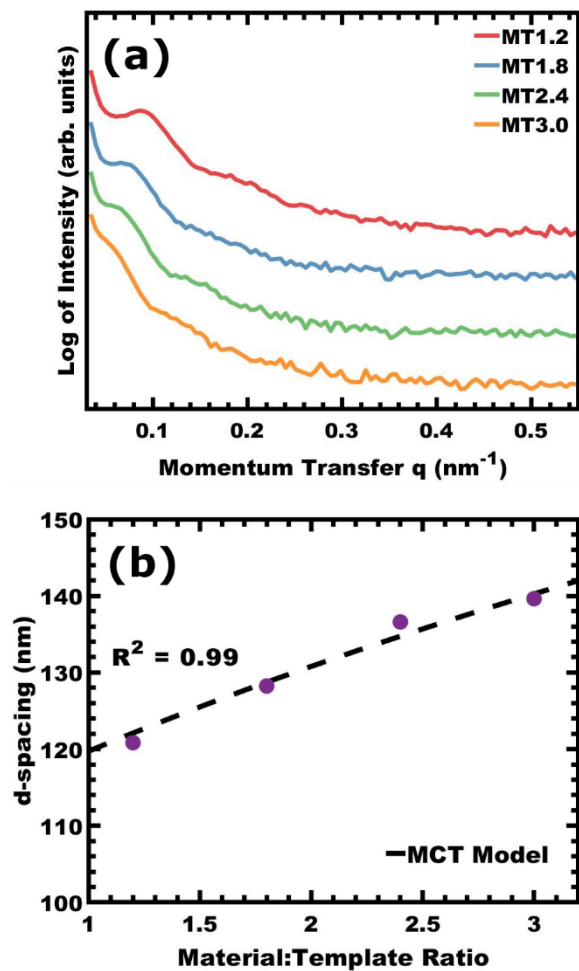
Figure 3. Representative SAXS data to characterize the average nanostructure for each sample in the series (a). Data are offset vertically for clarity. The trends in SAXS peak position (d-spacing=$2\pi/q$) as a function of the Material:Template ratio were well fitted by the MCT model (b).
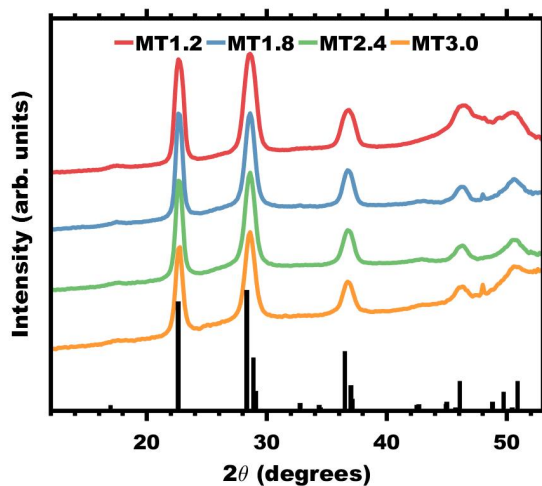
Figure 4. GI-WAXS data characterize the inorganic crystal structure for each sample condition in the series. The reference pattern corresponds to $T\text{-}Nb_2O_5$ (PDF No. 01-071-0336). Data were offset vertically for clarity. The peak at 47.3º (MT1.2, MT 1.8, and MT3.0) corresponds to the (220) peak of the Si substrate.
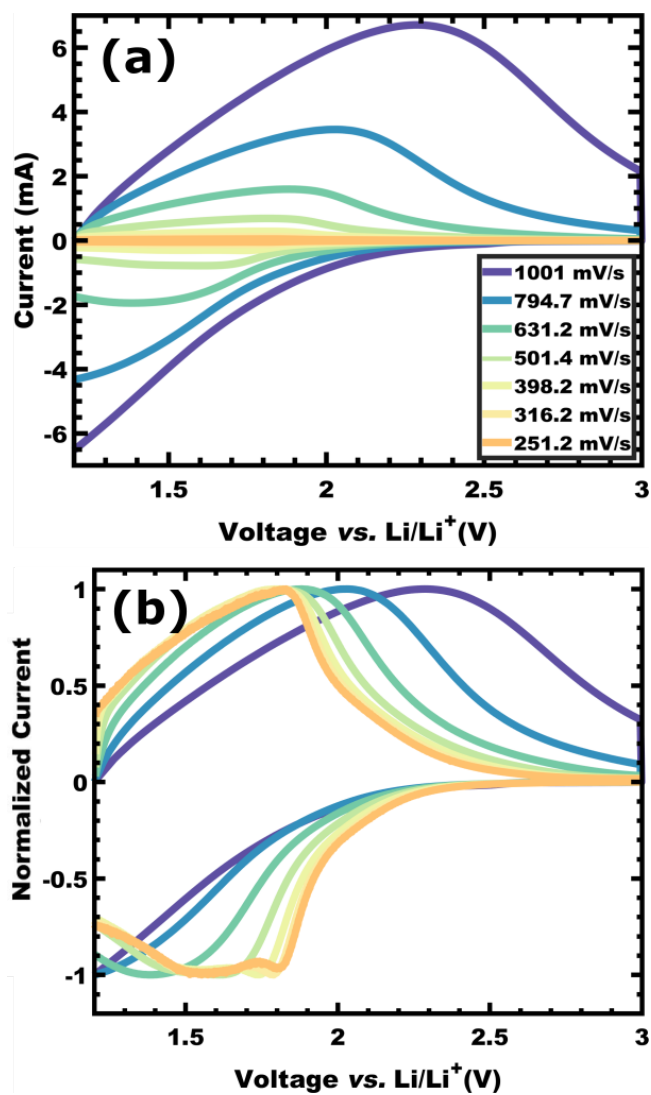
Figure 5. Cyclic voltammetry data from sample MT1.2 showing with logarithmically spaced sweep rates ranging from 250-1,000 mV s^{-1} (a). Normalization of this data (b) clarifies the corresponding peak shifts.
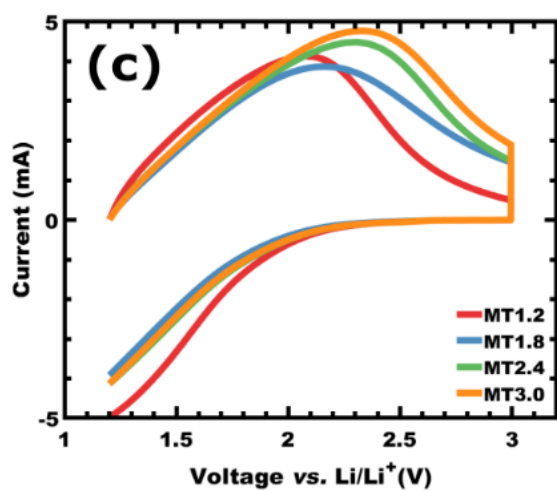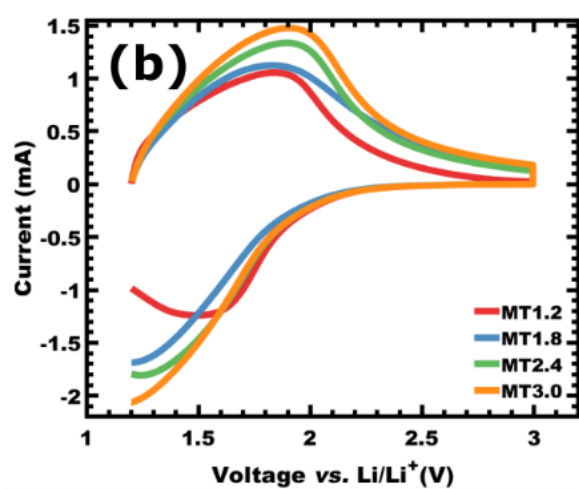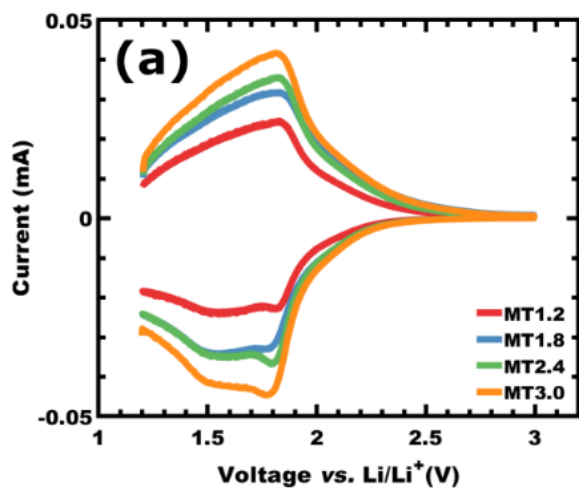
Figure 6. Comparison of cyclic voltammograms for the sample series at sweep rates of 2 mV s^{-1} (a), 100 mV s^{-1} (b), and 500 mV s^{-1} (c).
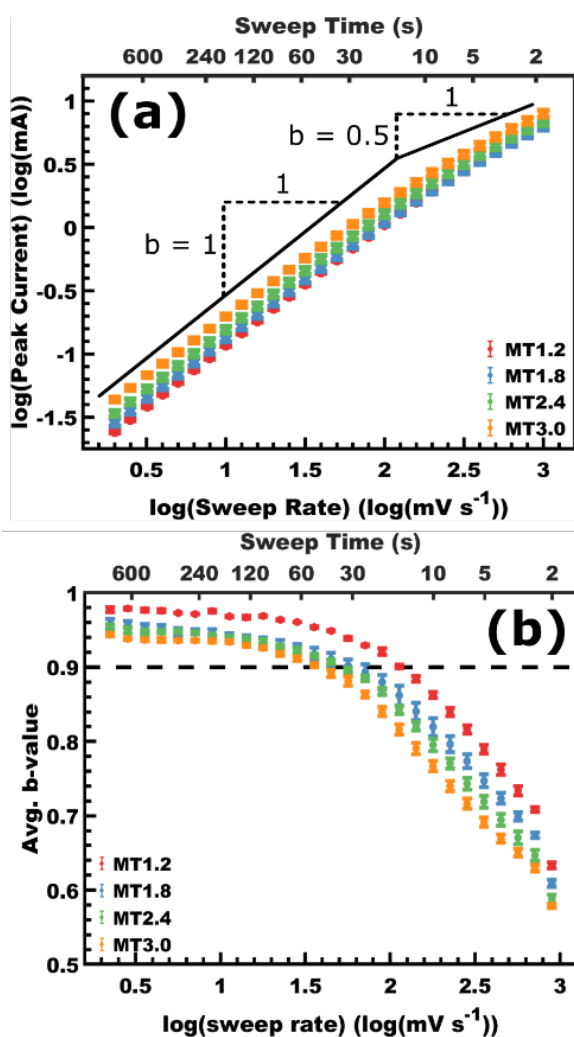
Figure 7. Rate-limiting step analysis was based upon the power-relationship between peak current and sweep rate. A log-log plot of the anodic peak current vs sweep rate for each sample condition is presented with characteristic slopes of 1.0 (surface limited) and 0.5 (diffusion limited) indicated (a). The derivative of panel a is termed the b-value and is plotted

in panel b. The dashed line at $b=0.9$ represents the Surface-Limited Threshold. Error bars

correspond to the standard-error-of-the-mean.
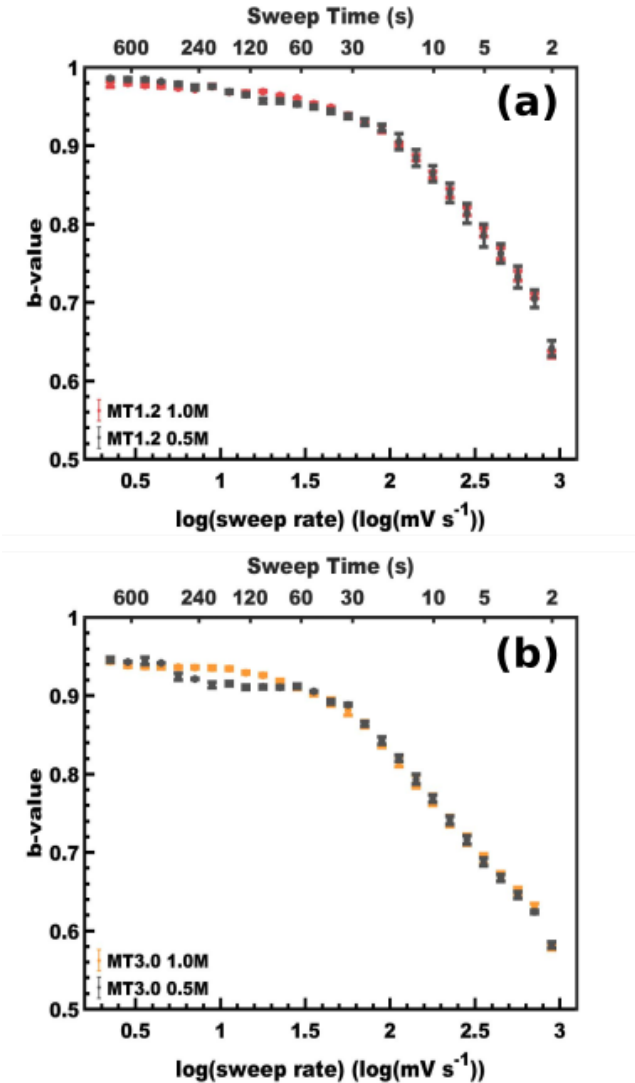
Figure 8. The sweep-rate dependent b-values were compared as a function of the LiClO$_4$

electrolyte concentration (0.5 and 1.0 M) for sample conditions MT1.2 (a) and MT3.0 (b).

Error bars correspond to the standard-error-of-the-mean.
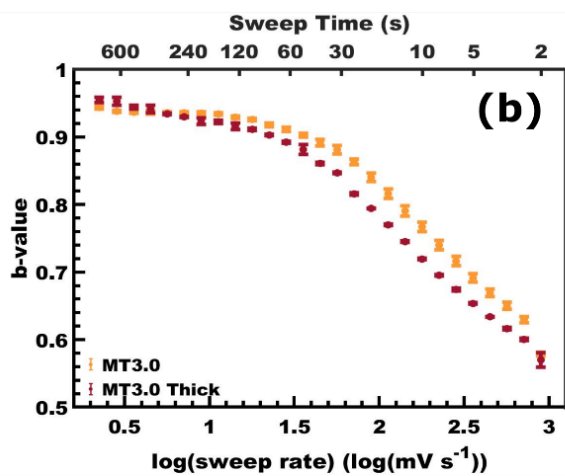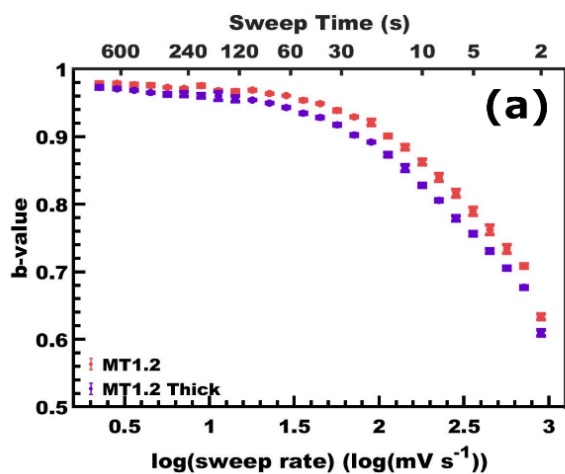
Figure 9. The sweep-rate dependent b-values were compared as a function of film thickness for sample conditions M:T1.2 (a) and M:T3.0 (b). Error bars correspond to the standard-error-of-the-mean.
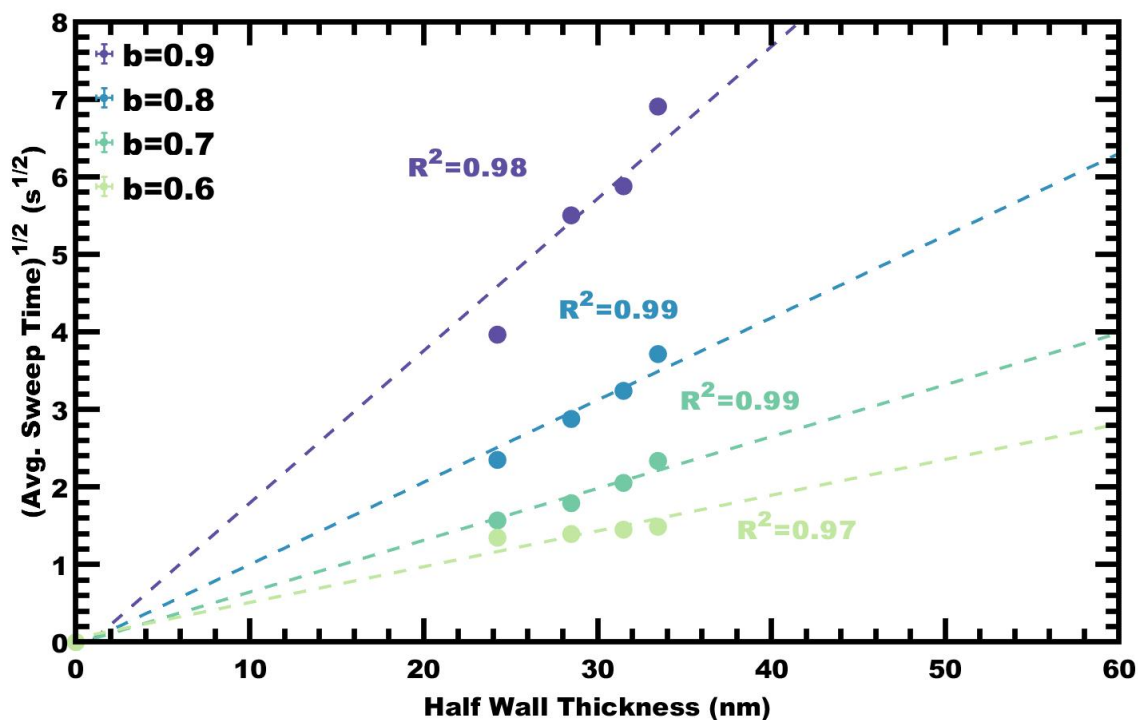
Figure 10. Plot correlating the intercalation length scale (half the wall thickness) to the square root of the average sweep time corresponding to specific b-values. Linear trends here are consistent with the generalized diffusion relationship of $x \propto \sqrt{(Dt)}$, where x is the diffusion length, t is time, and D is the diffusivity. Error bars correspond to the standard-error of each measure.

Schemes
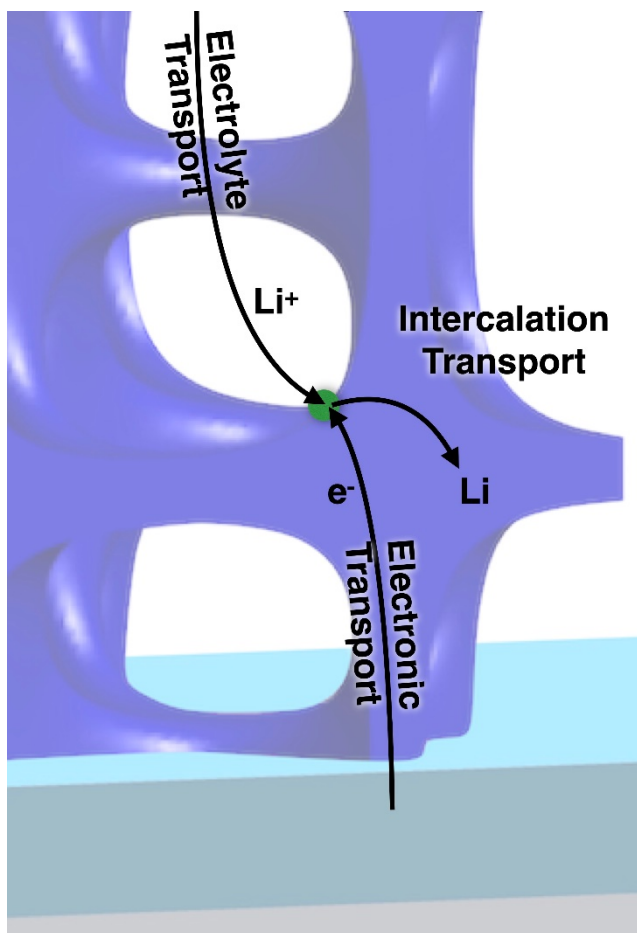
Scheme 1. The charging/discharging process involves three concomitant transport processes, including lithium intercalation into the wall thickness, ion transport through the electrolyte, and electron transport through the electrode. Ion insertion from the electrolyte to the electrode occurs at the interface. The rate-limiting step(s) could include any of the transport processes, which are diffusive in nature, or the insertion process which is surface limited. Each of these effects can be deconvolved using an architectural approach with minimal electrochemical modeling.

Tables

Table 1. Statistical measures from the isomorphic sample series including average values and the associated error as well as the dimension distributions of each architectural feature

Condition Name	Material-to-template ratio [M:T]	Average Pore Size [nm][a]	Pore Size Stdev. [nm][b]	Average Wall Thickness [nm][a]	Wall Thickness Stdev. [nm]	Crystallite Size [nm][c]	SAXS d-spacing [nm]	Porosity [vol%][d]
MT1.2	1.2	107.9 ± 1.7	23.8	48.5 ± 1.0	9.2	12.8	121.5	60%
MT1.8	1.8	104.7 ± 1.6	22.9	57.0 ± 1.1	10.0	12.7	129.5	47%
MT2.4	2.4	111.6 ± 1.7	24.1	63.0 ± 1.5	12.8	12.1	135.2	27%
MT3.0	3.0	111.0 ± 1.6	22.1	67.0 ± 1.1	10.2	11.7	139.6	10%

[a]The average values are reported ± the standard-error-of-the-mean (standard deviation divided by the square root of the number of measurements) to indicate the error of the mean value; [b] The standard deviation reflects the distribution width of the measured dimensions; [c]Crystallite size was determined using Scherrer analysis of the (001) peak; [d]Volume fractions of pores calculated from **SI eqn. 4.**

Table 2. Statistical measures of average film thickness as a function of spin-coating speed.

Condition Name	Spin-coating speed [rpm]	Film thickness [nm][a]	Sweep rate @ b = 0.9 [mV s⁻¹][b]	Sweep time [s][c]	Sweep rate @ b = 0.6 [mV s⁻¹][b]	Sweep time @b=0.6 [s][c]
MT1.2	1,000	80.4 ± 2.2	114.60 ± 0.48	15.70 ± 0.07	993.69 ± 38.63[4]	1.81 ± 0.07

MT1.2 (Thick)	400	91.0 ± 1.7	75.12 ± 0.22	23.93 ± 0.07	927.83 ± 28.10	1.94 ± 0.06
MT1.8	1,500	78.6 ± 2.7	59.48 ± 0.30	30.26 ± 0.15	926.73 ± 30.95[4]	1.94 ± 0.06
MT2.4	2,000	66.7 ± 1.4	52.13 ± 0.39	34.53 ± 0.26	856.71 ± 25.20	2.10 ± 0.06
MT3.0	2,150	65.2 ± 2.6	37.77 ± 0.27	47.66 ± 0.34	814.59 ± 26.23	2.21 ± 0.07
MT3.0 (Thick)	400	163.0 ± 4.9	24.02 ± 0.25	74.95 ± 0.77	714.77 ± 10.84	2.52 ± 0.04

[a]Average film thickness values are reported ± the standard-error-of-the-mean; [b]Sweep rate values were linearly interpolated between nearest experimental values in the lin-log coordinate space of Figure 8b. Sweep rate values are reported ± the bounding limits for error propagation based on Rolle's Theorem; [c]Sweep times were calculated as the voltage window divided by the sweep rate. Sweep time values are reported ± the error propagated from the sweep rate.